Highly Distorted Chiral Two-Dimensional Tin Iodide Perovskites for Spin Polarized Charge Transport

Haipeng Lu,[1] Chuanxiao Xiao,[1] Ruyi Song,[2] Tianyang Li,[2] Annalise E. Maughan,[1] Andrew Levin,[1] Roman Brunecky,[3] Joseph J. Berry,[1] David B. Mitzi,[2] Volker Blum,[2] and Matthew C. Beard*[,1]

[1] Chemistry & Nanoscience Center, National Renewable Energy Laboratory, Golden, Colorado 80401, United States

[2] Department of Mechanical Engineering and Material Science, Duke University, Durham, North Carolina 27708, United States

[3] Chemical and Bioscience Center, National Renewable Energy Laboratory, Golden, Colorado 80401, United States

Corresponding Author

Matthew C. Beard*: Matt.Beard@nrel.gov

ABSTRACT

Incorporating chiral organic molecules into organic/inorganic hybrid 2D-layered metal-halide perovskites results in a novel family of chiral hybrid semiconductors with unique spin-dependent properties. The embedded chiral organic moieties induce a chiroptical response from the inorganic metal-halide sublattice. However, the structural interplay between the chiral organic molecules and the inorganic sublattice, as well as their synergic effect on the resulting electronic band structure need to be explored in a broader material scope. Here we present three new layered tin iodide perovskites templated by chiral (*R*/*S*-)methylbenzylammonium (*R*/*S*-MBA), *i.e.* (*R*-/*S*-MBA)$_2$SnI$_4$, and their racemic phase (*rac*-MBA)$_2$SnI$_4$. These MBA$_2$SnI$_4$ compounds exhibit the largest level of octahedral bond distortion compared to any other reported layered tin iodide perovskite. The incorporation of chiral MBA cations leads to circularly polarized absorption from the inorganic Sn–I sublattice, displaying chiroptical activity in the 300–500 nm wavelength range. The bandgap and chiroptical activity are modulated by alloying Sn with Pb, in the series of (MBA)$_2$Pb$_{1-x}$Sn$_x$I$_4$. Finally, we show that vertical charge transport through oriented (*R*-/*S*-MBA)$_2$SnI$_4$ thin films is highly spin-dependent, arising from a chiral-induced spin selectivity (CISS) effect. We demonstrate a spin-polarization in the current-voltage characteristics as high as 94%. Our work shows the tremendous potential of these chiral hybrid semiconductors for controlling both spin and charge degrees of freedom.

Introduction

Hybrid organic-inorganic halide perovskites have emerged as revolutionary tunable semiconductors for photovoltaic and emergent optoelectronic applications.[1-4] The crystal structure of hybrid perovskite (ABX_3) consists of 3D corner-sharing metal-halide octahedra, with the A-site cations occupying voids within the cage formed by the BX_6 octahedral framework. The choice of the A-site cation for a stable perovskite structure is empirically determined in part by the Goldschmidt tolerance factor,[5] leading to rather limited structural diversity in the 3D metal-halide perovskite family. Two-dimensional layered metal-halide perovskites provide a much greater chemical and structural diversity, which allows an unprecedented control of their emergent properties.[6-10] For instance, many reports have shown that the optical,[11-13] electronic[14-16] and spin[17-19] properties of these 2D hybrid perovskite systems can be directly modulated by their organic/inorganic compositions, bond distortions and resulting crystal structures.

While these 2D hybrid semiconductors serve as a unique platform to study structure-property relationships, adding new degrees of complexity to the inorganic and/or organic component provides further access to new properties and functionalities. For instance, replacing the insulating aliphatic organic component with a semiconducting organic moiety results in various hybrid quantum well configurations with different electronic band alignments between the organic and inorganic sub-lattices. Such synergistic interaction leads to interesting optoelectronic applications.[20-22] Another interesting direction is to introduce chiral organic molecules into the hybrid semiconductor system. Researchers have shown that the chiral organics can effectively transfer a chirality response to the inorganic sublattice.[23,24] Several groups have demonstrated, for example, circularly polarized photoluminescence from these chiral hybrid semiconductors, suggesting they are promising candidates for spin-polarized LEDs.[25,26] Additionally, the chiral organic component can break the intrinsic centrosymmetry, making them promising scaffolds for nonlinear optics,[27-29] ferroelectricity,[30,31] and the bulk photovoltaic effect.[32] Recently, we developed a solution-processable spin-filter based upon a chiral 2D-layered hybrid perovskite, with the induced spin-selectivity arising from a chiral-induced spin selectivity (CISS) effect.[33] The spin-polarized current enhancement was as high as 86%. Clearly, adding chirality to these 2D-layered hybrid semiconductors opens the door to various exciting optoelectronic and spintronic devices for which controlling and modulating both spin and charge can be exploited. However, the material space of these chiral 2D hybrid semiconductors is still rather limited, and the generality of such chirality transfer and CISS effect needs to be investigated in a broader material scope.

Here we report the synthesis of two new chiral hybrid metal-halide perovskites, (*R*/*S*-)methylbenzylammonium tin iodide (*R*-/*S*-$MBA)_2SnI_4$, and the racemic analog (*rac*-$MBA)_2SnI_4$. The crystal structures adopt the corner-sharing 2D perovskite structure. Importantly, we find that the octahedra are among the most distorted known to date within the layered Sn–I perovskite family. The degree of distortion remains similar for both chiral and racemic versions of the perovskite structure, thereby enabling a well-defined comparison of the impact of chirality. Circular dichroism for (*R*-/*S*-$MBA)_2SnI_4$ samples indicates that the incorporation of the chiral

organic ammonium cations induces a chiroptical activity in the 300–500 nm wavelength range, *i.e.,* in the range of excitations stemming from the inorganic Sn–I sublattice. Templated by these chiral organics, alloyed samples (*R*-/*S*-MBA)$_2$Pb$_{1-x}$Sn$_x$I$_4$ (with input nominal Sn/Pb ratio x ranging from 0 to 1) were also prepared and this series displays tunable optical bandgaps with a bowing effect, for which the minimum observed bandgap occurs when x = 0.2. Interestingly, we find that the chiroptical activity can also be modulated by varying the alloy composition. Lastly, we demonstrate that vertical charge transport in these chiral 2D Sn–I perovskites depends sensitively on injected spin-polarization, obtaining a 94% current enhancement depending on the magnetization of a carrier-injecting tip.

Results and Discussion

Crystal Structure of Chiral (*R*-/*S*-MBA)$_2$SnI$_4$ and Racemic (*rac*-MBA)$_2$SnI$_4$. Single crystals of chiral (*R*-/*S*-MBA)$_2$SnI$_4$ and the racemic phase (*rac*-MBA)$_2$SnI$_4$ were grown from a concentrated hydroiodic acid solution, as adapted from our pervious report.[33] Orange, rod-like crystals were collected after a slow-cooling process from 90 °C to room temperature. Crystallographic data and structure refinement information appear in **Table 1**. The crystal structure consists of a layer of corner-sharing SnI_6^{4-} octahedra, with a bilayer of organic MBA cations separating the inorganic layers (**Figure 1**). The organic cation phenyl rings all align approximately parallel to the *b* axis and the chiral *R*-/*S*- and achiral *rac*- compounds display similar cell parameters. All three compounds crystallize in the orthorhombic system. The incorporation of the chiral MBA molecules results in a chiral space group $P2_12_12_1$ for (*R*-/*S*-MBA)$_2$SnI$_4$, while the racemic phase (*rac*-MBA)$_2$SnI$_4$ crystallizes in the centrosymmetric space group *Pnma*.

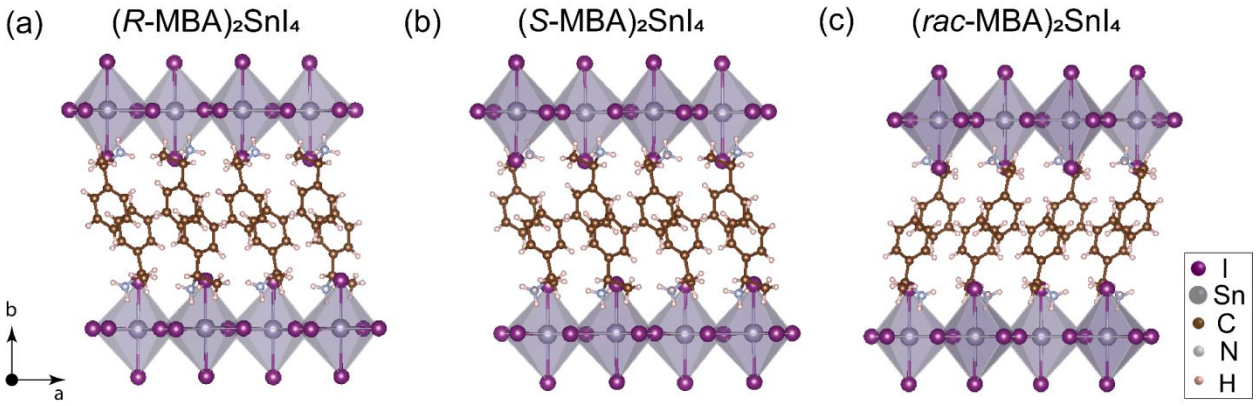

Figure 1. Crystal structure of (a) (*R*-MBA)$_2$SnI$_4$, (b) (*S*-MBA)$_2$SnI$_4$, and (c) (*rac*-MBA)$_2$SnI$_4$ from the side-view along the *c* direction. The axes shown correspond to all structures in a-c.

Table 1. Crystal Data and Structure Refinement for (*R*-MBA)$_2$SnI$_4$, (*S*-MBA)$_2$SnI$_4$, and (*rac*-MBA)$_2$SnI$_4$

	Compound Name		
	$(R\text{-MBA})_2SnI_4$	$(S\text{-MBA})_2SnI_4$	$(rac\text{-MBA})_2SnI_4$
Empirical formula	$C_{16}H_{24}N_2I_4Sn$	$C_{16}H_{24}N_2I_4Sn$	$C_{16}H_{24}N_2I_4Sn$
Crystal size (mm)	0.037×0.159×0.171	0.039×0.146×0.185	0.025×0.173×0.321
Formula weight		870.68	
Temperature		250 K	
Wavelength		0.71073 Å	
Crystal system		Orthorhombic	
Space group	$P2_12_12_1$	$P2_12_12_1$	*Pnma*
Unit cell dimensions	a = 8.9098(2) Å, b = 28.7413(6) Å, c = 9.3567(2) Å	a = 8.91262(19) Å, b = 28.7305(7) Å, c = 9.3578(2) Å	a = 8.7887(3) Å, b = 28.7381(9) Å, c = 9.4273(3) Å
Volume	2396.07(10) $Å^3$	2396.20(10) $Å^3$	2381.04(13) $Å^3$
Z	4	4	4
Density (calculated)	2.414 g/cm^3	2.413 g/cm^3	2.429 g/cm^3
Absorption coefficient	6.22 mm^{-1}	6.22 mm^{-1}	6.261 mm^{-1}
F(000)	1584	1584	1584
θ range for data collection	2.289 to 26.371°	2.289 to 26.372°	2.274 to 26.369°
Index ranges	-11<=h<=9, -35<=k<=35, -11<=l<=11	-11<=h<=10, -33<=k<=35, -11<=l<=10	-9<=h<=10, -35<=k<=33, -11<=l<=11
Reflections collected	24481	24777	14478
Independent reflections	4550 [R_{int} = 0.0217]	4502 [R_{int} = 0.0271]	2427 [R_{int} = 0.0252]
Completeness to θ = 25.242°	100%	100%	100%
Refinement method		Full-matrix least-squares on F^2	
Data / restraints / parameters	4897 / 0 / 212	4894 / 0 / 212	2477 / 0 / 111
Goodness-of-fit	1.091	1.141	1.122
Final R indices [I > 2σ(I)]	R_{obs} = 0.0160, wR_{obs} = 0.0183	R_{obs} = 0.0190, wR_{obs} = 0.0216	R_{obs} = 0.0204, wR_{obs} = 0.0238
R indices [all data]	R_{all} = 0.0326, wR_{all} = 0.0338	R_{all} = 0.0408, wR_{all} = 0.0415	R_{all} = 0.0460, wR_{all} = 0.0470
Largest diff. peak and hole	0.261 and -0.500 e·$Å^{-3}$	0.420 and -1.120 e·$Å^{-3}$	0.988 and -0.496 e·$Å^{-3}$

$R = \Sigma||F_o|-|F_c|| / \Sigma|F_o|$, $wR = \{\Sigma[w(|F_o|^2 - |F_c|^2)^2] / \Sigma[w(|F_o|^4)]\}^{1/2}$ and $w=1/[\sigma^2(Fo^2)+(0.0172P)^2+0.1141P]$ where $P=(Fo^2+2Fc^2)/3$

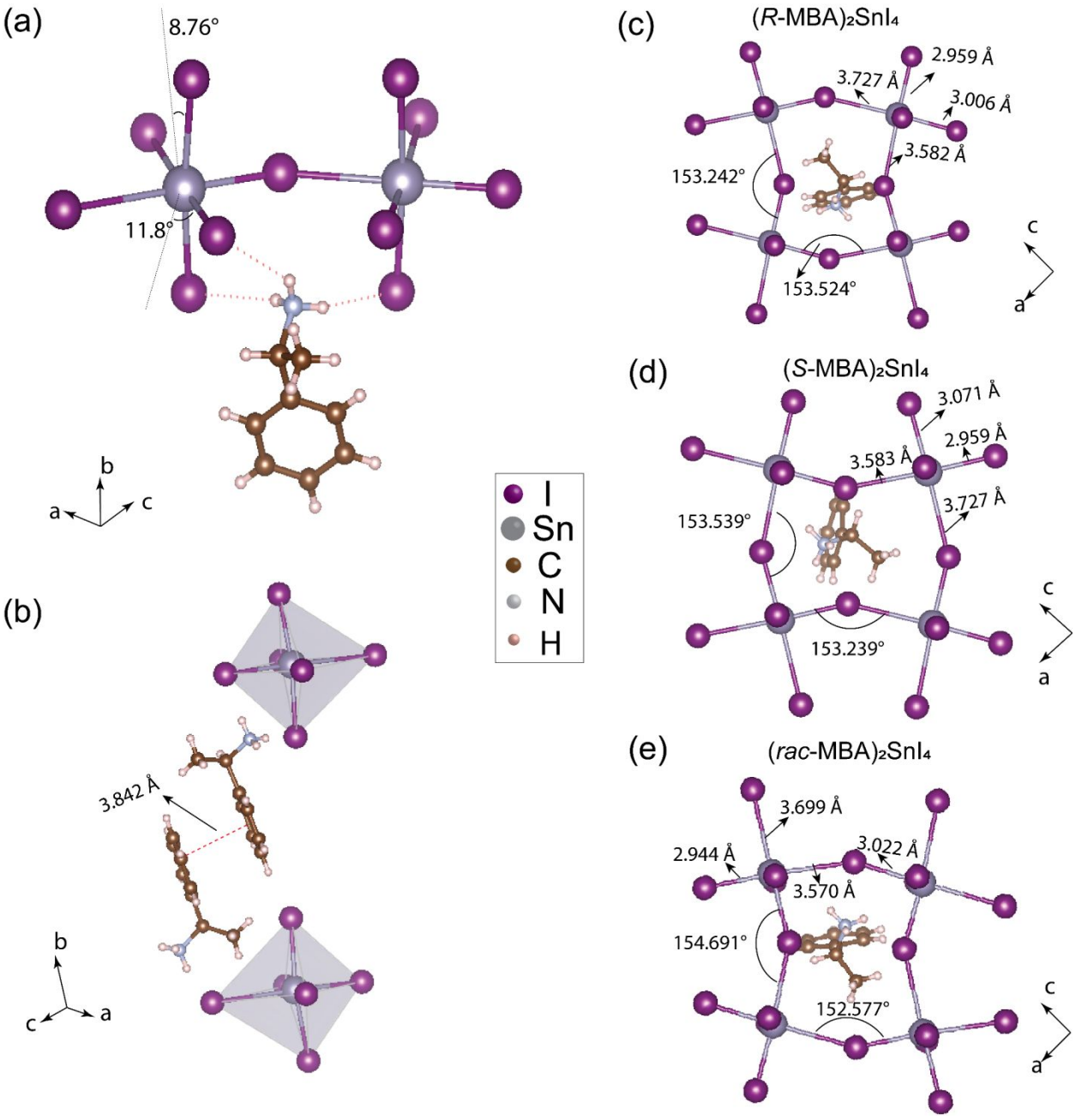

Figure 2. (a) Hydrogen bonds between the organic *R*-MBA cation and inorganic octahedra in (*R*-MBA)$_2$SnI$_4$. (b) π-π stacking of *R*-MBA cations along *b* direction. (c-e) Top-down view of crystal structures of (*R*-MBA)$_2$SnI$_4$, (*S*-MBA)$_2$SnI$_4$, and (*rac*-MBA)$_2$SnI$_4$, respectively. An in-plane distortion of the octahedra can be clearly observed.

The crystal packing and hydrogen bonds are similar in all three compounds. Taking (*R*-MBA)$_2$SnI$_4$ as an example, the organic MBA cations penetrate into the perovskite sheet (~ 0.45 Å[34]), with the ammonium head forming hydrogen bonds (N–H•••I) with two axial (N–H•••I$_a$: 2.75 and 2.94 Å)

and one equatorial (N–H•••I_e: 2.95 Å) iodide atoms (**Figure 2a**). The adjacent MBA cations along the stacking direction (*b* direction) interact closely by π–π stacking of benzene rings with a distance between ring centers of 3.842 Å (**Figure 2b**). The ammonium head deviates from the center of the cages in all three compounds (**Figure 2c-e**). The hydrogen bonds significantly distort the SnI_6^{4-} octahedra from an ideal configuration. In (*R*-MBA)$_2$SnI$_4$ (**Figure 2a**), the hydrogen bonds with the axial iodide atoms tilt the axial Sn–I bond by 8.76° from the ideal vertical axis. The axial Sn–I displays two bond distances (3.154 and 3.176 Å), with the longer one corresponding to the shorter N–H•••I_a distance, suggesting that strong hydrogen bonding is likely responsible for the axial bond tilting. While the out-of-plane distortion of the inorganic sheets is very small (<1°), there is significant in-plane rotation among the octahedra (**Figure 2c-e**). The hydrogen bonds with equatorial iodide atoms contribute to the in-plane tilting of the corner-shared octahedra since every bridged I atom is bounded to the ammonium head by N–H•••I_e.

(*R*-MBA)$_2$SnI$_4$ displays two in-plane Sn–I–Sn bond angles, namely 153.52° and 153.24°, both of which deviate significantly from 180° (ideal octahedra). The longest and shortest Sn–I bonds within an octahedron are both located within the equatorial directions, and the differences are as large as 0.77 Å. The average Sn–I bond distance is 3.267 Å, while the longest Sn–I bond is 3.727 Å, one of the longest bonds reported among tin iodide perovskites (such a bond-length can be considered semi-coordinated). To further quantify the degree of octahedral distortion, we calculated the bond length distortion index (*D*)[35] and bond angle variance (σ^2)[36] from

$$D = \frac{1}{6}\sum_{i=1}^{6}\frac{|d_i - d_0|}{d_0},$$

$$\sigma^2 = \frac{1}{11}\sum_{i=1}^{12}(\theta_i - 90)^2,$$

where d_i represents the individual Sn–I bond lengths, d_0 is the mean Sn–I bond distance, and θ_i corresponds to the octahedra I–Sn–I bond angles. For an ideal octahedron, both *D* and σ^2 are exactly 0. The larger the value of *D* and σ^2, the larger is the octahedra distortion. Interestingly, we find that these layered (MBA)$_2$SnI$_4$ perovskites exhibit the largest reported SnI_6 octahedron distortion index among values reported in literature (**Figure 3**). (*R*-MBA)$_2$SnI$_4$, (*S*-MBA)$_2$SnI$_4$ and (*rac*-MBA)$_2$SnI$_4$ show a distortion index of 0.079, 0.079 and 0.076 and bond angle variances of 10.37, 10.35, and 13.04 deg^2, respectively (**Supporting Information, Figure S1**). The level of structural distortion in *R*-, *S*-, and *rac*- compounds are very similar, and are significantly larger than other layered Sn–I perovskites[37] or their (MBA)$_2$PbI$_4$ analogs[23] (**Table S1**). The high degree of structural distortion of the (MBA)$_2$SnI$_4$ compounds directly results in unusual structural parameters relative to their Pb–I analogs. For instance, the in-plane lattice constants of (*R*-MBA)$_2$SnI$_4$ (a = 8.910 Å and c = 9.357 Å) are slightly larger than those of (*R-/S-/rac*-MBA)$_2$PbI$_4$ (*e.g.,* a = 8.868 Å and b = 9.247 Å in (*R*-MBA)$_2$PbI$_4$),[23] although they both possess the same crystal structure and the ionic radius of Sn^{2+} is smaller than that for Pb^{2+}. This ordering of bond lengths is in contrast with other

Sn–I and Pb–I series that are templated by the same organic cations, for which generally the in-plane lattice constants of the hybrid Sn halides are smaller than those of their Pb analogs (**Table S2**).

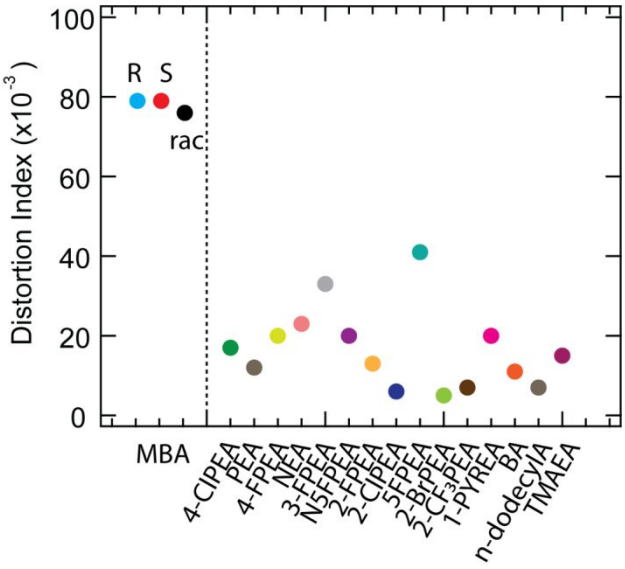

Figure 3. Bond length distortion indices (D) of (*R*-MBA)$_2$SnI$_4$, (*S*-MBA)$_2$SnI$_4$, and (*rac*-MBA)$_2$SnI$_4$ compounds, calculated based on the new reported crystal structures, with comparison to those of other reported[37] layered Sn–I perovskites.

Optical Properties of Chiral (*R*-/*S*-MBA)$_2$SnI$_4$ and Racemic (*rac*-MBA)$_2$SnI$_4$ Thin Films. To study the optical and chiroptical properties of these hybrid tin iodide compounds, we prepared polycrystalline thin films of (MBA)$_2$SnI$_4$ by spin casting a DMF solution of the corresponding crystals. Linear absorption shows an absorption peak at 408 nm and a shoulder peak at 452 nm, which extends to ~500 nm. *R*-, *S*- and *rac*- films display no obvious differences in linear absorption spectra (**Figure 4a**). It is interesting to note that there is no obvious sharp exciton peak in these MBA$_2$SnI$_4$ compounds, which is in contrast to that of other layered tin iodide perovskites templated by achiral organics (*e.g.* PEA$_2$SnI$_4$)[17] or chiral MBA$_2$PbI$_4$ thin films[33]. We hypothesize that the loss of the distinct excitonic transition may be associated with the exceptionally high degree of structural distortion, but the precise mechanism still needs to be further investigated. Transmission circular dichroism (CD) measurements show distinct CD signals from 300–500 nm for (*R*-MBA)$_2$SnI$_4$ and (*S*-MBA)$_2$SnI$_4$ thin films, while (*rac*-MBA)$_2$SnI$_4$ displays no CD (**Figure 4b**). All the CD peaks are at the same wavelengths (at 357, 402, 443, and 473 nm) with opposite signs for (*R*-MBA)$_2$SnI$_4$ and (*S*-MBA)$_2$SnI$_4$ thin films. It is notable that none of these chiroptically active transitions are from the organic component, which only absorbs in the range of 200–300 nm. In fact, these chiroptical transitions (at 402 and 443 nm, for example) correlate fairly well with their linear absorption peaks (at 408 and 452 nm respectively), indicating that the optical

transitions originating from the inorganic sublattice acquire a chiral response. We also observe the Cotton effect near the bandedge electronic transitions (at 443 and 473 nm) in the chiral films, which is very similar to our previous chiral Pb analogs[33]. Clearly, the incorporation of the chiral molecules has enabled the chiral optical activity of the electronic transition within the inorganic Sn–I sublattice.

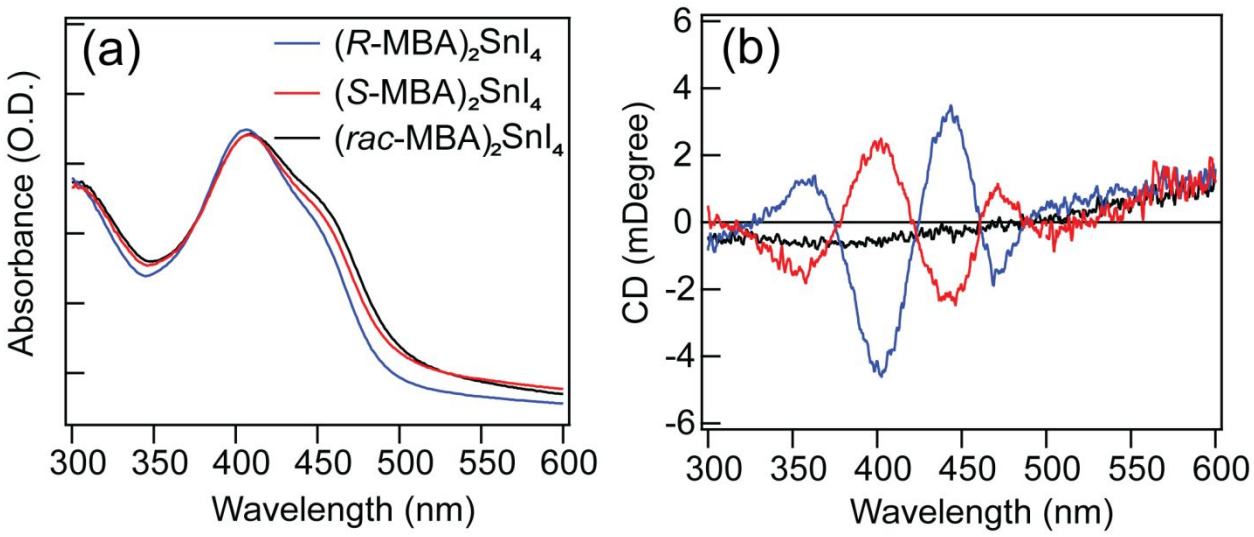

Figure 4. (a) Linear absorption and (b) circular dichroism (CD) spectra of (*R*-MBA)$_2$SnI$_4$, (*S*-MBA)$_2$SnI$_4$, and (*rac*-MBA)$_2$SnI$_4$ thin films. CD spectra display derivative features at 300 to 500 nm, with *R*- and *S*- showing the opposite signs.

Tunable Optoelectronic Properties of (*R*-MBA)$_2$Pb$_{1-x}$Sn$_x$I$_4$ (x = 0 – 1). To better examine the influence of the electronic properties of the inorganic sublattice on their chiroptical properties, we prepared a series of single-crystal Pb/Sn alloyed 2D perovskites (*R*-/*S*-MBA)$_2$Pb$_{1-x}$Sn$_x$I$_4$ (x = 0 – 1). Note that x value only represents the input nominal Sn/Pb ratio, while actual elemental composition is determined by EDS (**Table S3**). We hypothesize that, when templated by the MBA cations, the electronic properties can be systematically modulated by metal alloying, thereby tuning their chiroptical properties. Powder XRD data of (*R*-MBA)$_2$Pb$_{1-x}$Sn$_x$I$_4$ (input composition: x = 0, 0.05, 0.20, 0.50, 0.80, 1) show similar crystallinity and crystal pattern across the whole solid solution composition. Pawley refinements of the orthorhombic structure (space group $P2_12_12_1$) against the powder diffraction data suggest that all synthesized crystals of intermediate composition crystallize in the same space group, as shown in **Figure S2a**. The lattice parameters extracted from the Pawley fits are shown in **Figure S2b**.We note that the in-plane lattice parameters (a and c) increase slightly with increasing Sn content, which is consistent with our single crystal data that indicate (*R*-MBA)$_2$SnI$_4$ has a larger lattice volume than (*R*-MBA)$_2$PbI$_4$. In contrast, the b lattice parameter corresponding to the stacking direction of the perovskite layers remains relatively unchanged across the series. These data indicate that the large distortion of the

SnI_6 octahedra manifests across the alloyed specimens and is further responsible for the larger lattice volumes observed in the Sn-rich members of the series.

Linear optical properties of the powders were measured by diffuse reflectance spectroscopy. Optical bandgaps were extracted based on the absorption onsets from the Kubelka-Munk absorption spectra ($\alpha/S = (1-R)^2/(2R)$, where α is absorption coefficient, S is scattering coefficient, and R is the absolute reflectance) (**Figure 5a**). The absorption spectra show sharp absorption edges suggesting direct bandgap semiconductors. Both $(R\text{-MBA})_2PbI_4$ and $(R\text{-MBA})_2Pb_{0.95}Sn_{0.05}I_4$ display characteristic excitonic peaks due to the strong dielectric confinement within the inorganic wells, but the sharp excitonic feature is no longer apparent for higher Sn concentrations. To better analyze the bandgap change upon Sn alloying, we fit the absorption spectra using a 2D generalized Elliot model (**SI**),[38] where the bandgap associated with exciton and the fundamental bandedge can be estimated. We find that both the exciton and bandgap display an anomalous trend in the alloyed samples. The bandgap (E_g) is initially reduced when adding more Sn to the $(R\text{-MBA})_2PbI_4$ compounds, but the trend is not monotonic with increasing Sn content as expected from Vegard's law. Instead, there is a significant bandgap bowing effect in $(R\text{-MBA})_2Pb_{1-x}Sn_xI_4$, with the minimum value found at an input $x = 0.2$ (*exciton*) and $x = 0.5$ (*bandgap*) (**Figure 5b**). Both the pure Pb and Sn compounds exhibit a higher bandgap than do their intermediates. This bowing trend, i.e. the onset of optical absorption is lower than the associated endpoints, can also be visually observed from the color of the as-grown crystals. Crystals of both $x = 0$ and $x = 1$ exhibit a yellow color, while their intermediate solid solutions display red to dark-red colors (**Figure 5b**, inset). Furthermore, the apparent bowing documented in **Figure 5b** is clearly outside variations in exciton binding energy and associated exciton absorption features that occur across the pure-Pb (large exciton binding energy) to pure Sn (low and no apparent excitonic absorption) systems. The anomalous E_g trend is similar to that observed in the 3D $CH_3NH_3Sn_{1-x}Pb_xI_3$[39,40] systems as well as for some 2D perovskites systems.[41] The bowing effect is generally attributed to the energy mismatch between *s* and *p* orbitals of Pb and Sn forming predominantly Sn/I-derived valence band maximum (VBM) and predominantly Pb/I-derived conduction band minimum (CBM) in the intermediates.[42] Below, we show by first-principles calculations that the apparent bowing also appears in the band structure calculations of ordered alloy models and thus, is likely a consequence of shifts of the fundamental gap of the alloyed compounds and not (as discussed above) a results of variations in exciton binding energy.

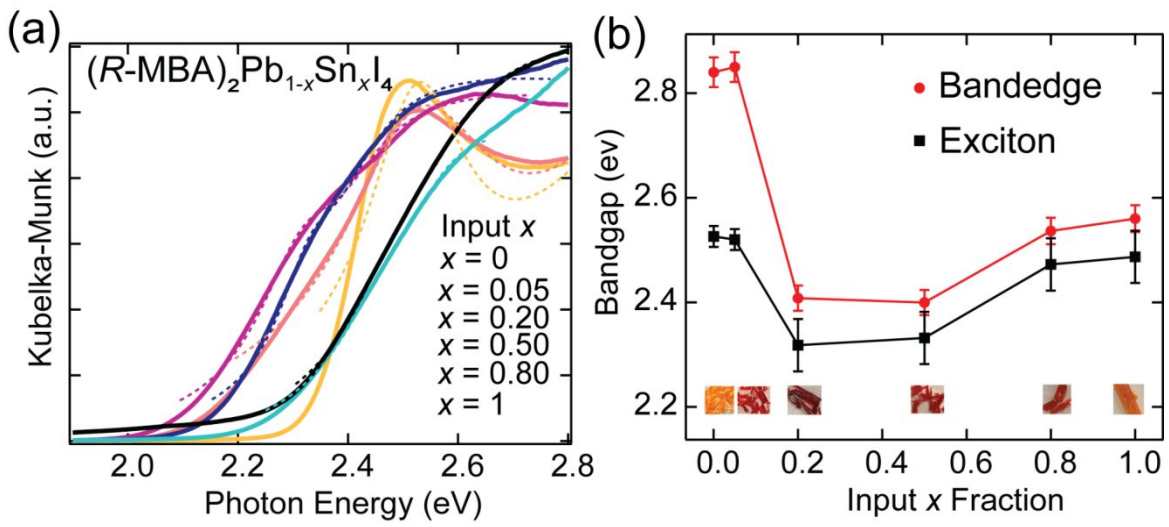

Figure 5. (a) Optical absorption of freshly-prepared crystalline samples of $(R\text{-MBA})_2Pb_{1-x}Sn_xI_4$ (input x = 0, 0.05, 0.20, 0.50, 0.80, 1), obtained from diffuse reflectance spectroscopy. Dash lines are the best-fit model based upon a 2D Elliot equation. (b) Best-fit values of the exciton energy and the bandgap of the solid solution powders as a function of input Sn fraction. Inset images are corresponding photographs of crystals. The errors associated with optical bandgaps are extracted from the fitting of the absorption onset in (a).

To understand the electronic structure in the alloyed (*i.e.,* mixed Sn/Pb) compounds and elucidate the observed band bowing, we performed DFT-based first-principles calculations on locally ordered models of $(S\text{-MBA})_2Pb_{1-x}Sn_xI_4$ (x = 0, 0.25, 0.5, 0.75, 1; note that the observed optical bandgaps of *R*- and *S*- are exactly the same) based on the all-electron electric structure code FHI-aims[43-46] (see Method section for more details). Input geometries for x = 0 and 1 are from single crystal X-ray experiments while for x = 0.25, 0.5, and 0.75 they are generated by substituting a corresponding proportion of the metallic atoms in either $(S\text{-MBA})_2PbI_4$ or $(S\text{-MBA})_2SnI_4$ crystal structures, depending on which is more similar to the target composition. Additionally, for x = 0.25 and 0.75, we doubled the unit cell size by two, along the (a, c) plane, including four Sn/Pb sites in each inorganic layer to accommodate the same stoichiometry in each plane (see **Figure S3** and **Figure S4** as well as small, schematic insets in **Figure 6d**). For each modeled compound, atomic positions and unit cell vectors were based on the semi-local DFT (PBE[47] generalized-gradient approximation including the Tkatchenko-Scheffler (TS) van der Waals correction[48], PBE+TS for short). Computationally optimized lattice parameters are within 2.2% of the experimental geometries. Computationally relaxed inorganic layer bond angles remain within 5° of the above-described input geometries (**Table S4**, **Figure S5** and **Figure S6**). **Figure 6a** shows the unit cell of $(S\text{-MBA})_2SnI_4$ and **Figure 6b** shows its Brillouin zone in reciprocal space. For qualitatively reliable band structures, a more demanding level of theory is needed (see Methods). Hybrid DFT-HSE06 electronic band structures including spin-orbit coupling (SOC, *i.e.*, DFT-HSE06+SOC[46]) of $(S\text{-MBA})_2Pb_{1-x}Sn_xI_4$ (x = 0, 0.25, 0.5, 0.75, 1) and contributions from Sn (cyan), Pb (magenta) and I (green) to each band are shown in **Figure 6c**. The largest supercell models considered here

(x = 0.25 and 0.75) contain 376 atoms overall and require the use of a supercomputer for DFT-HSE06+SOC. For the eight lowest-lying conduction states as well as the eight highest-lying valence states, the Mulliken decompositions underlying the elemental fractions in **Figure 6c** are reported in detail in the SI (**Figures S8-9)**. For all five systems, the frontier orbitals are formed by the inorganic moiety, resulting in type Ib quantum wells.[49]

Figure 6d shows the modulation of the computationally predicted, fundamental band gaps across different compositions of Pb/Sn alloys. Interestingly, (S-MBA)$_2$PbI$_4$ has a larger bandgap than (S-MBA)$_2$SnI$_4$ (2.17eV versus 2.02eV) and a pronounced bowing effect, caused by alloying. Since the computed gaps do not include excitonic effects (unlike the measured optical spectra reported in **Figure 5b**), the experimentally observed trend between the pure Pb / pure Sn end points is thus already found in the computed fundamental gaps. The Mulliken decompositions of the states forming the energy bands reveals that the Pb atoms contribute significantly to the lowest unoccupied states, while Sn species are the more significant cation contributors to the highest-lying occupied states (**Figure S7**) (both the VBM and CBM also contain pronounced contributions from the halide ions). A systematic energy shift between more Pb-derived bands vs. more Sn derived bands in the same unit cell is thus the most likely origin of the observed band bowing.

As a function of overall composition, the band bowing trend is reproduced qualitatively, but not quantitatively, between the experimentally found bandgaps in **Figure 5b** and the computationally reported fundamental gaps in **Figure 6d**. In particular, the pronounced compositional asymmetry of the experimental gaps is not seen in the computed gaps. However, in the computations, only fully ordered, idealized structure models could be considered due to their already demanding system size. The comparison of computed results and experiment suggests that the local distributions of Sn versus Pb atoms in the real samples could be different from the ideal order assumed in the computations and/or that the Sn/Pb ratios in real samples could deviate from the input nominal ratio (see EDS results in **Table S3** as well as additional computational models in **Figure S10** and associated text). For example, the experimentally observed variation would be consistent with the idea that the *onset* of absorption in the alloyed samples is determined by local mixed Sn/Pb areas with compositions between $0.25 < x < 0.75$, whereas the average band gap inferred from fitting absorption spectra in **Figure 5b** and/or the overall color of the samples may vary more, depending on the degree of overall sample inhomogeneity.

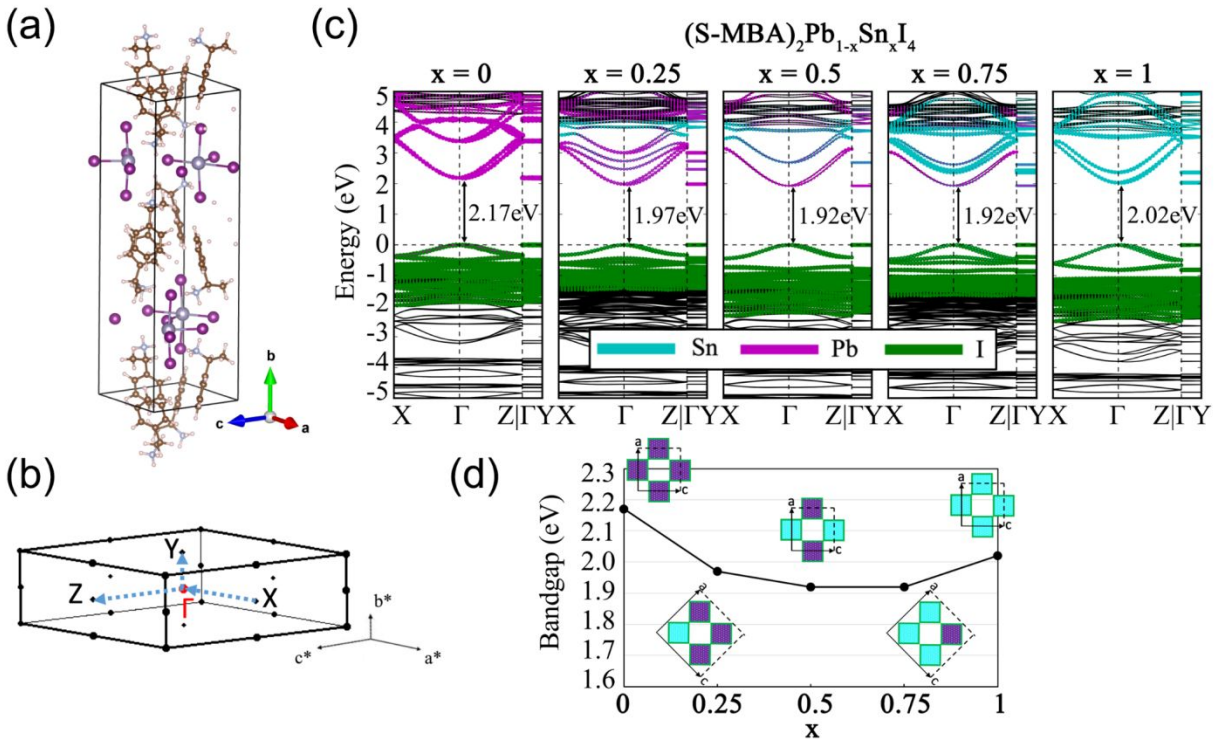

Figure 6. (a), (b)Representative unit cell of the (*S*-MBA)$_2$SnI$_4$ crystal structure in real space and the k-path with its first Brillouin zone in reciprocal space used for band plotting in (c). (c)The computed DFT-HSE06+SOC electronic band structures of (*S*-MBA)$_2$Pb$_{1-x}$Sn$_x$I$_4$ (x = 0, 0.25, 0.5, 0.75, 1). The contributions of electronic states to the bands are identified for Sn (cyan), Pb (magenta), I (green) and organic-derived states (black). (d) Plots of the theoretical bandgaps with respect to the ratio of Sn as metallic atoms in the perovskite. Inset pictures illustrate the input Pb/Sn ratios, where purple squares represent Pb and cyan squares represent Sn.

The optical and chiroptical properties of the (*R*-MBA)$_2$Pb$_{1-x}$Sn$_x$I$_4$ solid solution was further studied by spin casting a DMF solution of corresponding crystals. Linear absorption spectra of thin films show similar absorption features as powder samples (**Figure 7a**). For instance, both (*R*-MBA)$_2$PbI$_4$ and (*R*-MBA)$_2$Pb$_{0.95}$Sn$_{0.05}$I$_4$ exhibit a characteristic exciton peak at ~498 nm, while other compositions (x = 0.20, 0.50, 0.80, and 1) do not show distinct exciton peaks. The absorption onset of (*R*-MBA)$_2$Pb$_{0.80}$Sn$_{0.20}$I$_4$ also appears to be the lowest energy among all compositions. The crystalline texture of these films is further characterized by XRD (**Figure 7b**). XRD data display exclusively (0 *2k* 0) peaks, indicating that these 2D Sn–I perovskite layers are highly oriented parallel to the substrate, similar to their Pb analogs. Additionally, there is minimum to no shift with XRD peaks between different compositions, which is consistent with powder diffraction data, as well as, with the computed lattice parameters. This is because the observed peaks represent the interlayer distance between inorganic sheets, which is mostly defined by the organic layers and thus essentially unchanged.

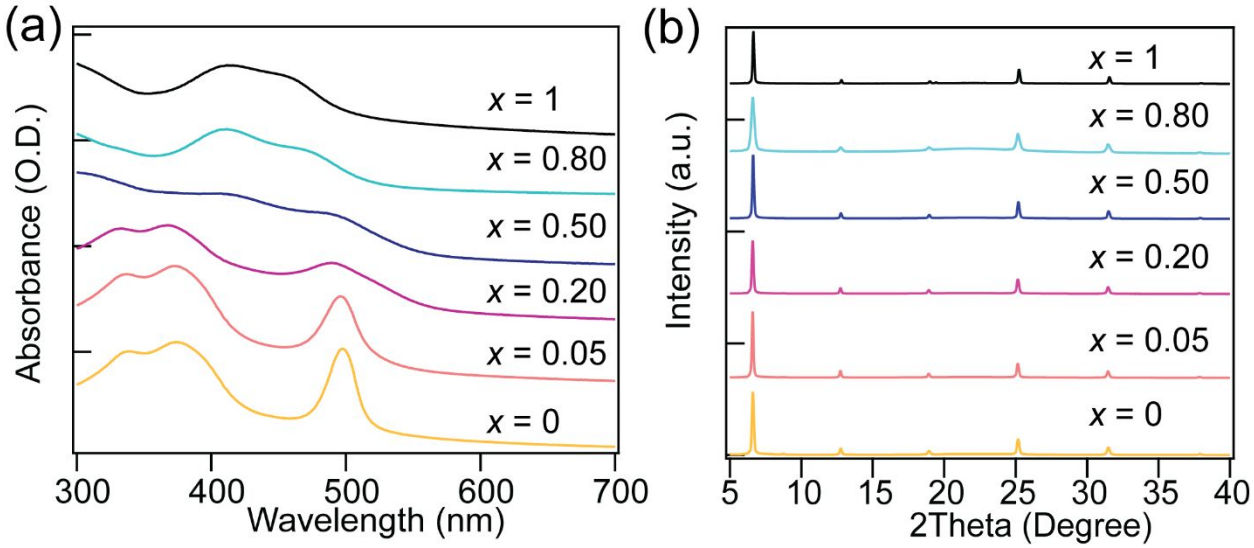

Figure 7. Linear absorption (a) and XRD (b) of (R-MBA)$_2$Pb$_{1-x}$Sn$_x$I$_4$ (x = 0, 0.05, 0.20, 0.50, 0.80, 1) solid solution thin films.

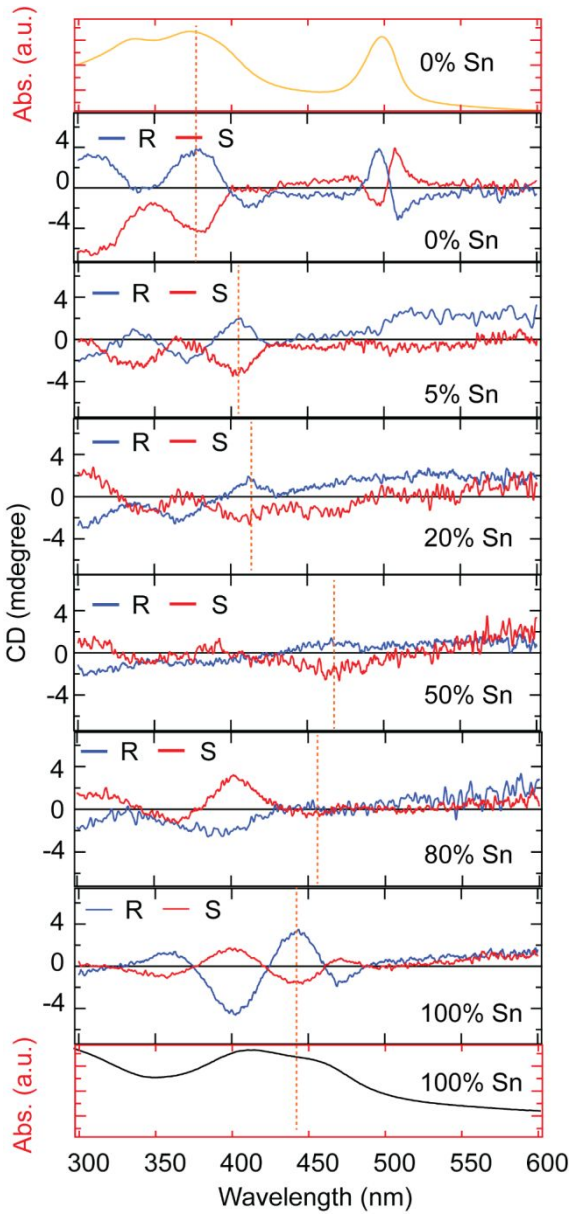

Figure 8. CD spectra of $(R\text{-MBA})_2Pb_{1-x}Sn_xI_4$ (x = 0, 0.05, 0.20, 0.50, 0.80, 1) solid solution thin films (Blue: *R*-perovskite; Red: *S*-perovskite), overlapped with the linear absorption spectra of two ends, *i.e.* $(MBA)_2PbI_4$ and $(MBA)_2SnI_4$, on the top and bottom, respectively. Orange dash lines indicate the shift of peaks.

To further illustrate how the tunable electronic structures can modulate their chiroptical properties, we performed CD measurements on $(R\text{-MBA})_2Pb_{1-x}Sn_xI_4$ (x = 0, 0.05, 0.20, 0.50, 0.80, 1) thin films (**Figure 8**). The CD spectra clearly show peak shifts across the whole range of $(R\text{-MBA})_2Pb_{1-x}Sn_xI_4$ ($x = 0-1$), with *R*- and *S*- compounds displaying bisignate features with opposite signs. The chiroptical properties of chiral $(R\text{-}/S\text{-MBA})_2PbI_4$ have been thoroughly discussed in our previous report,[33] characterized by distinct derivative features near the bandedge (at 497 and 508 nm) resulting from the Cotton effect. Interestingly, these derivative peaks near the bandedge

disappear upon mixing with Sn even at a 5% concentration level. Therefore, to better analyze the shift of the CD spectra, we focus on the second lowest energy peak (orange dashed-line). We follow the shift of these peaks assuming that the same handedness of hybrid compounds should result in the same sign (positive or negative) for that CD peak across all solid solution compositions, since the same chirality would perturb that electronic transition in the same manner. The second lowest energy peak clearly shows a redshift from 380 to 406, 413, and 466 nm when the Sn concentration is increased from 0, to 5, 20, and 50%, respectively (orange dashed-line). When Sn concentration is further increased to 80 and 100%, we find a blueshift of the CD peaks. The shift in CD peaks is thus consistent with the observed bandgap bowing in the optical measurements, as well as the computed results. Therefore, the CD spectra can be tuned in (R-MBA)$_2$Pb$_{1-x}$Sn$_x$I$_4$ (x = 0, 0.05, 0.20, 0.50, 0.80, 1) solid solution, pointing to the modulation of chiroptical properties by tuning the electronic structures of these chiral hybrid semiconductors.

Chiral Induced Spin Selectivity (CISS) Based on (R-/S-MBA)$_2$SnI$_4$. To investigate the CISS effect in these chiral Sn–I compounds, we performed magnetic conductive-probe atomic force microscopy (mCP-AFM) measurements on (R-/S-MBA)$_2$SnI$_4$ thin films. The (R-/S-MBA)$_2$SnI$_4$ films were prepared by spin casting a DMF solution of crystals on FTO-coated glass substrates. Compared to their chiral Pb-analogs, the chiral Sn–I films appear to be much more conductive likely due in part to the spontaneous p-type doping of the Sn–I crystals[6,50,51]. In this study, we applied bias from –1.2 to 1.2 V and measured the vertical current transport through the chiral organic/inorganic sublattices for different AFM tip magnetizations. When the AFM tip is magnetized by a permanent external magnet, the spin-degeneracy of carriers in the tip is lifted, so that only one spin-state is predominately injected into the thin film. CISS introduces an addition spin scattering effect for carriers and thus increases the resistance for carriers with a particular spin orientation. Based on the difference in the measured J-V characteristics under the opposite tip magnetization directions, we define the degree of spin polarization, P,[52] for the current in the system during vertical charge transport.

$$P = \frac{I_+ - I_-}{I_+ + I_-} \times 100\%$$

Where I_+ and I_- are the measured currents at –1 V when the tip magnetic field is pointing up or down, respectively. We obtained a highly spin-polarized current, P of +94%, in the (R-MBA)$_2$SnI$_4$ film, which is slightly higher than what we previously reported in an analogous (R-MBA)$_2$PbI$_4$ film. In contrast, the (S-MBA)$_2$SnI$_4$ film yields a spin polarization of –93%. The small difference in the measured spin-polarized current between (R-MBA)$_2$PbI$_4$ and (R-MBA)$_2$SnI$_4$ thin films suggests that spin-dephasing within in the inorganic sublattice (caused by large spin-orbit coupling from the heavy Pb or Sn atoms) likely is not significant in these self-assembled chiral organic/inorganic structures. Thus, the spin-polarized current is mostly attributed to the effect of the spin-filtering from the oriented chiral organic molecules (increased resistance to carriers with the incorrect spin orientation). Here the transport requires carriers to transverse many layers.

Previously, we found that to achieve nearly 100% spin-polarization the carriers would need to transport through ~ 60–80 nm of the oriented chiral layers. The degree of spin-orbit coupling in a typical oriented chiral organic molecule has been found to be related to the number of turns of the helical potential.[53-55] Here, it appears each oriented layer contributes to the overall polarized current likely in similar manner as that for each turn of a much longer oriented chiral molecule. But, the exact impact of each individual layer is not yet determined, nor the spin-scattering that might occur within the inorganic layers. Ongoing work in our laboratories is exploring these features.

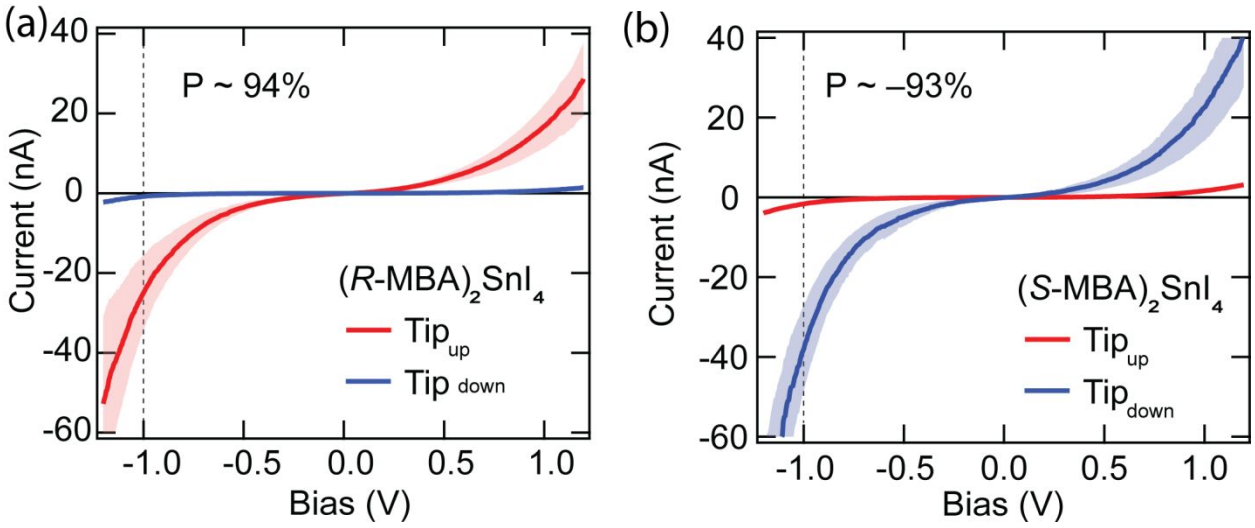

Figure 9. Room-temperature *I-V* curves obtained using the magnetic conductive-probe AFM technique of chiral 2D hybrid (*R*-MBA)$_2$SnI$_4$ (a) and (*S*-MBA)$_2$SnI$_4$ thin films (b, ~50–60 nm thick). The *J-V* response for each 2D film was averaged over 100 scans at different points (raw data in **Figure S12**), and the shaded region around the lines marks the 95% confidence limits for the average results.

Conclusion

In conclusion, we report three new 2D tin iodide layered perovskites templated by chiral and achiral MBA cations, *i.e.* (*R*-MBA)$_2$SnI$_4$, (*S*-MBA)$_2$SnI$_4$ and (*rac*-MBA)$_2$SnI$_4$. Single crystal structure analysis shows that these three compounds consist of highly distorted octahedra, in response to specific hydrogen bonding arrangements. Indeed, the distortion index is the largest among all reported layered tin iodide perovskites. When templated by chiral organic cations, (*R*-MBA)$_2$SnI$_4$ and (*S*-MBA)$_2$SnI$_4$ crystallize in a chiral space group ($P2_12_12_1$), while their racemic analog crystallizes in an achiral space group (*Pnma*). The organic cation chirality further results in circularly polarized absorption from the inorganic Sn–I sublattice, which shows chiroptical activity in the 300–500 nm wavelength range. When the Sn is alloyed with Pb, the optical bandgap can be

readily tuned, exhibiting a bowing effect, which is also supported by theoretical computation of the fundamental gaps. Additionally, the CD spectra can be modulated by tuning the composition of $(R\text{-MBA})_2Pb_{1-x}Sn_xI_4$ alloys. Similar to Pb analogs, thin films of these chiral 2D tin iodide perovskites can work as effective spin filters, with a spin polarization of 94%. Our study demonstrates the tremendous potential of bridging organic chirality with inorganic semiconductors for applications where spin, charge and light are coupled and controllable.

Methods

Materials. All chemicals were used as received unless otherwise indicated. (*R*)-(+)-α-methylbenzylamine (*R*-MBA, 98%, ee 96%), (*S*)-(−)-α-methylbenzylamine, (*S*-MBA, 98%, ee 98%), (±)-α-methylbenzylamine (*rac*-MBA, 99%), lead oxide (PbO, 99.999%), *N,N*-anhydrous DMF, 57% w/w aqueous hydriodic acid (HI) solution (99.95%, distilled, stabilized by H_3PO_2), and 50% w/w aqueous hypophosphorous acid solution were purchased from Sigma-Aldrich. Tin (Ⅳ) oxide (SnO_2, 99.9%) was purchased from Alfa-Aesar, and it was grinded using a mortar pestle before synthesis, which significantly helps to dissolve in HI/H_3PO_2 solution.

Synthesis of (*R*-/*S*-/*rac*-MBA)$_2$SnI$_4$ single crystals. The synthesis of 2D chiral Sn–I perovskite single crystals was adapted from our previous report.[33] All syntheses in the work are performed in air. Briefly, 135 mg of grinded SnO_2 (0.896 mmol), 200 μl (1.57 mmol) of *R*-, *S*-, or *rac*-MBA, 5.5 ml of HI, and 0.5 ml H_3PO_2 solution were loaded into a glass vial. The mixture was then stirred at 120 °C until all solids were dissolved, yielding a clear yellow solution. The vial was subsequently transferred to an oil bath at 90 °C, followed by a slow cooling process with a cooling rate of 1 °C/hour, giving orange rods. These crystals were carefully filtered in a N_2 box and dried in vacuum overnight.

Synthesis of (R-MBA)$_2$Pb$_{1-x}$Sn$_x$I$_4$ (x = 0 – 1) single crystals. Synthesis of solid solution (R-MBA)$_2$Pb$_{1-x}$Sn$_x$I$_4$ (x = 0 – 1) single crystals is similar to pure $(MBA)_2SnI_4$ crystals. In general, different molar ratios of SnO_2 and PbO ($r_{Sn:Pb}$ = 0:1, 0.05:0.95, 0.20:0.80, 0.50:0.50, 0.80:0.20, 1:0, total of 0.896 mmol) were mixed with 200 μl (1.57 mmol) of *R*-MBA, 5.5 ml of HI, 0.5 ml H_3PO_2 solution in a glass vial. The mixture was stirred at 120 °C until all solids were dissolved, followed by a slow cooling process in an oil bath from 90 °C to room temperature. Orange to dark red needle crystals were collected in a N_2 box by vacuum filtration. The final products were dried in vacuum overnight. The actual elemental composition was analyzed by EDS for these crystals (**Table S3**).

Preparation of (*R*-/*S*-/*rac*-MBA)$_2$SnI$_4$ and (R-MBA)$_2$Pb$_{1-x}$Sn$_x$I$_4$ thin films. Glass, quartz or FTO substrates were washed sequentially using acetone and isopropanol in a sonicator for 100 min each, followed by an ultraviolet-ozone treatment for 15 min. Precursor solutions were prepared by dissolving crystals in DMF with 10 wt% (*e.g.* 20 mg in 200 μl) and were immediately used. Thin films were prepared by spin coating the corresponding precursor solution onto substrates using a spin rate of 4000 rpm for 30 s, followed by thermal annealing at 100 °C for 10 min. Thin films on glass substrates were used for XRD measurements. Thin films on quartz substrates were used for linear optical and CD measurements. Thin films on FTO were used for mCP-AFM measurements.

Powder and single crystal X-ray diffraction. Laboratory powder X-ray diffraction measurements were collected on a Rigaku DMax 2200 diffractometer with a rotating Cu anode. Single crystals of each member of the series were ground into powders in an agate mortar and pestle and were affixed to glass slides using

a thin layer of vacuum grease. Samples containing tin were prepared in an Argon-filled glove box and kept under inert atmosphere until the measurement was performed to prevent oxidation.

Pawley refinements were performed using the least-squares method implemented in GSAS/EXPGUI.[56,57] The refinements were initialized using the crystal structure of R-MBA_2SnI_4 determined from single-crystal X-ray diffraction measurements in this work, and the lattice parameters and profile broadening terms were allowed to refine independently.

Single crystal diffraction data were collected on a Rigaku XtaLAB Synergy-S instrument at 250K using Mo Kα radiation (λ = 0.71073 Å). A full sphere of diffraction data was collected and multi-scan empirical absorption correction was applied. Structure solution was obtained by direct methods using the SHELXS program and refined using the least-squares method by employing the SHELXL[58] program within the Olex2 software[59].

Linear optical absorption measurements. For powder absorption, powder samples were first obtained by grinding single crystals using mortar and pestle. Linear optical absorption spectra were obtained by performing optical diffuse reflectance measurements in a Cary 5000 UV-vis-NIR spectrometer operating in the 800 – 200 nm region at room temperature. $BaSO_4$ was used as the reference of 100% reflectance, and to dilute powder samples for all measurements. Linear optical absorption spectra of powders were generated by converting reflectance to absorption data using the Kubelka-Munk equation[60]: $\alpha/S = (1 - R)^2/(2R)$, where R is the reflectance and α and S are the absorption and scattering coefficients, respectively. Bandgaps of layered perovskites were then calculated by a linear fitting of the absorption onsets. For thin film absorption, absorption spectra were collected in the transmission mode using a quartz substrate as the reference of 100% transmittance.

CD measurements. CD measurements were performed using a Jasco J-715 spectropolarimeter with the thin film placed in the beam path. The spectra obtained were averages of 3–5 scans. The CD spectra were collected in the 200 – 600 nm wavelength range and with 0.2 nm resolution.

First-principles calculations. The all-electron electronic structure code FHI-aims[43] was employed to perform the first-principles density functional theory (DFT) calculations and numeric atom-centered orbital (NAO) basis sets were used in all calculations. Lattice parameter and atomic coordinates were relaxed towards local minima of the Born-Oppenheimer potential energy surface using semi-local Perdew-Burke-Ernzerhof (PBE)[47] functional plus the Tkatchenko-Scheffler (TS) pairwise dispersion scheme for van der Waals (vdW) interactions[48]. For the geometry optimization, FHI-aims' "tight" numerical defaults and **k**-point grids ($4 \times 2 \times 4$) for the unexpanded unit cells (x=0,0.5,1) and ($3 \times 2 \times 3$) for the doubled unit cells (x=0.25,0.75) were employed. This level of theory has been shown to reliably predict the structure of complex, layered hybrid organic-inorganic perovskites in the past.[49] Regarding electronic band structures, DFT-GGA suffers from the electronic delocalization error[61] and may lead to large underestimation of the bandgap or even wrong ordering of the states[62]. We chose to employ the hybrid DFT functional Heyd-Scuseria-Ernzerhof (HSE06, with 25% Hartree-Fock exchange and a screening parameter of 0.11 $bohr^{-1}$),[63,64] which has been found to offer a good balancing between computational cost and accuracy for hybrid organic-inorganic perovskites (HOIPs)[21,49,65,66]. In addition, second-variational non-self-consistent spin-orbit coupling (SOC)[46] within FHI-aims was also included in band calculations. For the hybrid DFT band structure calculations, FHI-aims "intermediate" numerical defaults and k-grid ($3 \times 3 \times 3$) were used.

AFM measurements. The AFM topography images (**Figure S11**) were acquired via a Bruker Icon AFM system. The scans are in peakforce mode using a "scananalysis-air" tip. The scan size is 1 um, with 1024 points in fast-axis, 256 lines in slow axis. The depth profile was taken by vertically scratching the sample surface with a new blade. The EDS measurements were performed on a Hitachi 4800 SEM platform. The

electron beam condition was 20 kV, 5 μA. When doing SEM mapping, the electron beam condition was 3 kV, 2 μA.

C-AFM measurements. The conductive-AFM measurements were performed via a Bruker Icon AFM system in an Ar-filled glovebox. The tip used in this work is "Bruker MESP-V2" in contact mode. We pre-magnetized the Co-Cr coated tips by a strong permanent magnetic for ~1 hour and then performed the scans immediately. During the measurement, the tip was virtually grounded, the voltages were applied to the sample. The voltage ramp is from -1.2 V to 1.2 V, with a scan rate of 0.3 Hz. More than 100 *I-V* curves were taken from different locations on each sample for each condition, with the tip magnetized by different field orientations (magnetic south, north, no magnetic).

Associated Content

Supporting Information. Single crystal XRD data, powder XRD data and Pawley refinements, DFT computation and AFM data can be found in SI. The crystal structure of (*R*-MBA)$_2$SnI$_4$, (*S*-MBA)$_2$SnI$_4$ and (*rac*-MBA)$_2$SnI$_4$ had been deposited as CIF files into the CCDC database with the number of 1994337, 1994338, 1994336, respectively.

Notes

The authors declare no competing financial interest.

Acknowledgement

We gratefully acknowledge support from the Center for Hybrid Organic Inorganic Semiconductors for Energy (CHOISE) an Energy Frontier Research Center funded by the Office of Basic Energy Sciences, Office of Science within the U.S. Department of Energy through contract number DE-AC36-08G028308. The views expressed in the article do not necessarily represent the views of the DOE or the U.S. Government. The U.S. Government retains and the publisher, by accepting the article for publication, acknowledges that the U.S. Government retains a nonexclusive, paid-up, irrevocable, worldwide license to publish or reproduce the published form of this work, or allow others to do so, for U.S. Government purposes.

References

(1) Kojima, A.; Teshima, K.; Shirai, Y.; Miyasaka, T. Organometal Halide Perovskites as Visible-Light Sensitizers for Photovoltaic Cells. *Journal of the American Chemical Society* **2009**, *131*, 6050-6051.

(2) Lee, M. M.; Teuscher, J.; Miyasaka, T.; Murakami, T. N.; Snaith, H. J. Efficient Hybrid Solar Cells Based on Meso-Superstructured Organometal Halide Perovskites. *Science* **2012**, *338*, 643.

(3) Li, Z.; Klein, T. R.; Kim, D. H.; Yang, M.; Berry, J. J.; van Hest, M. F. A. M.; Zhu, K. Scalable fabrication of perovskite solar cells. *Nature Reviews Materials* **2018**, *3*, 18017.

(4) Fu, Y.; Zhu, H.; Chen, J.; Hautzinger, M. P.; Zhu, X. Y.; Jin, S. Metal halide perovskite nanostructures for optoelectronic applications and the study of physical properties. *Nature Reviews Materials* **2019**, *4*, 169-188.

(5) Goldschmidt, V. M. Die Gesetze der Krystallochemie. *Naturwissenschaften* **1926**, *14*, 477-485.

(6) Mitzi, D. B.; Feild, C. A.; Harrison, W. T. A.; Guloy, A. M. Conducting tin halides with a layered organic-based perovskite structure. *Nature* **1994**, *369*, 467-469.

(7) Mao, L.; Stoumpos, C. C.; Kanatzidis, M. G. Two-Dimensional Hybrid Halide Perovskites: Principles and Promises. *Journal of the American Chemical Society* **2019**, *141*, 1171-1190.

(8) Zhang, F.; Lu, H.; Tong, J.; Berry, J. J.; Beard, M.; Zhu, K. Advances in Two-Dimensional Organic-Inorganic Hybrid Perovskites. *Energy & Environmental Science* **2020**, *13*, 1154-1186.

(9) Mitzi, D. B. Templating and structural engineering in organic–inorganic perovskites. *Journal of the Chemical Society, Dalton Transactions* **2001**, 1-12.

(10) Saparov, B.; Mitzi, D. B. Organic–Inorganic Perovskites: Structural Versatility for Functional Materials Design. *Chemical Reviews* **2016**, *116*, 4558-4596.

(11) Smith, M. D.; Karunadasa, H. I. White-Light Emission from Layered Halide Perovskites. *Accounts of Chemical Research* **2018**, *51*, 619-627.

(12) Li, T.; Chen, X.; Wang, X.; Lu, H.; Yan, Y.; Beard, M. C.; Mitzi, D. B. Origin of Broad-Band Emission and Impact of Structural Dimensionality in Tin-Alloyed Ruddlesden–Popper Hybrid Lead Iodide Perovskites. *ACS Energy Letters* **2020**, *5*, 347-352.

(13) Mao, L.; Wu, Y.; Stoumpos, C. C.; Wasielewski, M. R.; Kanatzidis, M. G. White-Light Emission and Structural Distortion in New Corrugated Two-Dimensional Lead Bromide Perovskites. *Journal of the American Chemical Society* **2017**, *139*, 5210-5215.

(14) Pedesseau, L.; Sapori, D.; Traore, B.; Robles, R.; Fang, H.-H.; Loi, M. A.; Tsai, H.; Nie, W.; Blancon, J.-C.; Neukirch, A.; Tretiak, S.; Mohite, A. D.; Katan, C.; Even, J.; Kepenekian, M. Advances and Promises of Layered Halide Hybrid Perovskite Semiconductors. *ACS Nano* **2016**, *10*, 9776-9786.

(15) Grancini, G.; Nazeeruddin, M. K. Dimensional tailoring of hybrid perovskites for photovoltaics. *Nature Reviews Materials* **2019**, *4*, 4-22.

(16) Katan, C.; Mercier, N.; Even, J. Quantum and Dielectric Confinement Effects in Lower-Dimensional Hybrid Perovskite Semiconductors. *Chemical Reviews* **2019**, *119*, 3140-3192.

(17) Chen, X.; Lu, H.; Li, Z.; Zhai, Y.; Ndione, P. F.; Berry, J. J.; Zhu, K.; Yang, Y.; Beard, M. C. Impact of Layer Thickness on the Charge Carrier and Spin Coherence Lifetime in Two-Dimensional Layered Perovskite Single Crystals. *ACS Energy Letters* **2018**, *3*, 2273-2279.

(18) Giovanni, D.; Chong, W. K.; Dewi, H. A.; Thirumal, K.; Neogi, I.; Ramesh, R.; Mhaisalkar, S.; Mathews, N.; Sum, T. C. Tunable room-temperature spin-selective optical Stark effect in solution-processed layered halide perovskites. *Science Advances* **2016**, *2*, e1600477.

(19) Zhai, Y.; Baniya, S.; Zhang, C.; Li, J.; Haney, P.; Sheng, C.-X.; Ehrenfreund, E.; Vardeny, Z. V. Giant Rashba splitting in 2D organic-inorganic halide perovskites measured by transient spectroscopies. *Science Advances* **2017**, *3*, e1700704.

(20) Mitzi, D. B.; Chondroudis, K.; Kagan, C. R. Design, Structure, and Optical Properties of Organic−Inorganic Perovskites Containing an Oligothiophene Chromophore. *Inorganic Chemistry* **1999**, *38*, 6246-6256.

(21) Dunlap-Shohl, W. A.; Barraza, E. T.; Barrette, A.; Dovletgeldi, S.; Findik, G.; Dirkes, D. J.; Liu, C.; Jana, M. K.; Blum, V.; You, W.; Gundogdu, K.; Stiff-Roberts, A. D.; Mitzi, D. B. Tunable internal quantum well alignment in rationally designed oligomer-based perovskite films deposited by resonant infrared matrix-assisted pulsed laser evaporation. *Materials Horizons* **2019**, *6*, 1707-1716.

(22) Gao, Y.; Shi, E.; Deng, S.; Shiring, S. B.; Snaider, J. M.; Liang, C.; Yuan, B.; Song, R.; Janke, S. M.; Liebman-Peláez, A.; Yoo, P.; Zeller, M.; Boudouris, B. W.; Liao, P.; Zhu, C.; Blum, V.; Yu, Y.; Savoie, B. M.; Huang, L.; Dou, L. Molecular engineering of organic–inorganic hybrid perovskites quantum wells. *Nature Chemistry* **2019**, *11*, 1151-1157.

(23) Billing, D. G.; Lemmerer, A. Synthesis and crystal structures of inorganic–organic hybrids incorporating an aromatic amine with a chiral functional group. *CrystEngComm* **2006**, *8*, 686-695.

(24) Ahn, J.; Lee, E.; Tan, J.; Yang, W.; Kim, B.; Moon, J. A new class of chiral semiconductors: chiral-organic-molecule-incorporating organic–inorganic hybrid perovskites. *Materials Horizons* **2017**, *4*, 851-856.

(25) Long, G.; Jiang, C.; Sabatini, R.; Yang, Z.; Wei, M.; Quan, L. N.; Liang, Q.; Rasmita, A.; Askerka, M.; Walters, G.; Gong, X.; Xing, J.; Wen, X.; Quintero-Bermudez, R.; Yuan, H.; Xing, G.; Wang, X. R.; Song, D.; Voznyy, O.; Zhang, M.; Hoogland, S.; Gao, W.; Xiong, Q.; Sargent, E. H. Spin control in reduced-dimensional chiral perovskites. *Nature Photonics* **2018**, *12*, 528-533.

(26) Ma, J.; Fang, C.; Chen, C.; Jin, L.; Wang, J.; Wang, S.; Tang, J.; Li, D. Chiral 2D Perovskites with a High Degree of Circularly Polarized Photoluminescence. *ACS Nano* **2019**, *13*, 3659-3665.

(27) Yuan, C.; Li, X.; Semin, S.; Feng, Y.; Rasing, T.; Xu, J. Chiral Lead Halide Perovskite Nanowires for Second-Order Nonlinear Optics. *Nano Letters* **2018**, *18*, 5411-5417.

(28) Peng, Y.; Yao, Y.; Li, L.; Wu, Z.; Wang, S.; Luo, J. White-light emission in a chiral one-dimensional organic–inorganic hybrid perovskite. *Journal of Materials Chemistry C* **2018**, *6*, 6033-6037.

(29) Moon, T. H.; Oh, S.-J.; Ok, K. M. [((R)-C8H12N)4][Bi2Br10] and [((S)-C8H12N)4][Bi2Br10]: Chiral Hybrid Bismuth Bromides Templated by Chiral Organic Cations. *ACS Omega* **2018**, *3*, 17895-17903.

(30) Yang, C.-K.; Chen, W.-N.; Ding, Y.-T.; Wang, J.; Rao, Y.; Liao, W.-Q.; Tang, Y.-Y.; Li, P.-F.; Wang, Z.-X.; Xiong, R.-G. The First 2D Homochiral Lead Iodide Perovskite Ferroelectrics: [R- and S-1-(4-Chlorophenyl)ethylammonium]2PbI4. *Advanced Materials* **2019**, *31*, 1808088.

(31) Hu, Y.; Florio, F.; Chen, Z.; Phelan, W. A.; Siegler, M. A.; Zhou, Z.; Guo, Y.; Hawks, R.; Jiang, J.; Feng, J.; Zhang, L.; Wang, B.; Wang, Y.; Gall, D.; Palermo, E. F.; Lu, Z.; Sun, X.; Lu, T.-M.; Zhou, H.; Ren, Y.; Wertz, E.; Sundararaman, R.; Shi, J. A chiral switchable photovoltaic ferroelectric 1D perovskite. *Science Advances* **2020**, *6*, eaay4213.

(32) Huang, P.-J.; Taniguchi, K.; Miyasaka, H. Bulk Photovoltaic Effect in a Pair of Chiral–Polar Layered Perovskite-Type Lead Iodides Altered by Chirality of Organic Cations. *Journal of the American Chemical Society* **2019**, *141*, 14520-14523.

(33) Lu, H.; Wang, J.; Xiao, C.; Pan, X.; Chen, X.; Brunecky, R.; Berry, J. J.; Zhu, K.; Beard, M. C.; Vardeny, Z. V. Spin-dependent charge transport through 2D chiral hybrid lead-iodide perovskites. *Science Advances* **2019**, *5*, eaay0571.

(34) Du, K.-z.; Tu, Q.; Zhang, X.; Han, Q.; Liu, J.; Zauscher, S.; Mitzi, D. B. Two-Dimensional Lead(II) Halide-Based Hybrid Perovskites Templated by Acene Alkylamines: Crystal Structures, Optical Properties, and Piezoelectricity. *Inorganic Chemistry* **2017**, *56*, 9291-9302.

(35) Baur, W. The geometry of polyhedral distortions. Predictive relationships for the phosphate group. *Acta Crystallographica Section B* **1974**, *30*, 1195-1215.

(36) Robinson, K.; Gibbs, G. V.; Ribbe, P. H. Quadratic Elongation: A Quantitative Measure of Distortion in Coordination Polyhedra. *Science* **1971**, *172*, 567.

(37) Knutson, J. L.; Martin, J. D.; Mitzi, D. B. Tuning the Band Gap in Hybrid Tin Iodide Perovskite Semiconductors Using Structural Templating. *Inorganic Chemistry* **2005**, *44*, 4699-4705.

(38) Campi, D.; Coriasso, C. Optical nonlinearities in multiple quantum wells: Generalized Elliott formula. *Physical Review B* **1995**, *51*, 10719-10728.

(39) Hao, F.; Stoumpos, C. C.; Chang, R. P. H.; Kanatzidis, M. G. Anomalous Band Gap Behavior in Mixed Sn and Pb Perovskites Enables Broadening of Absorption Spectrum in Solar Cells. *Journal of the American Chemical Society* **2014**, *136*, 8094-8099.

(40) Ogomi, Y.; Morita, A.; Tsukamoto, S.; Saitho, T.; Fujikawa, N.; Shen, Q.; Toyoda, T.; Yoshino, K.; Pandey, S. S.; Ma, T.; Hayase, S. CH3NH3SnxPb(1–x)I3 Perovskite Solar Cells Covering up to 1060 nm. *The Journal of Physical Chemistry Letters* **2014**, *5*, 1004-1011.

(41) Mao, L.; Tsai, H.; Nie, W.; Ma, L.; Im, J.; Stoumpos, C. C.; Malliakas, C. D.; Hao, F.; Wasielewski, M. R.; Mohite, A. D.; Kanatzidis, M. G. Role of Organic Counterion in Lead- and Tin-Based Two-Dimensional Semiconducting Iodide Perovskites and Application in Planar Solar Cells. *Chemistry of Materials* **2016**, *28*, 7781-7792.

(42) Goyal, A.; McKechnie, S.; Pashov, D.; Tumas, W.; van Schilfgaarde, M.; Stevanović, V. Origin of Pronounced Nonlinear Band Gap Behavior in Lead–Tin Hybrid Perovskite Alloys. *Chemistry of Materials* **2018**, *30*, 3920-3928.

(43) Blum, V.; Gehrke, R.; Hanke, F.; Havu, P.; Havu, V.; Ren, X.; Reuter, K.; Scheffler, M. Ab initio molecular simulations with numeric atom-centered orbitals. *Computer Physics Communications* **2009**, *180*, 2175-2196.

(44) Levchenko, S. V.; Ren, X.; Wieferink, J.; Johanni, R.; Rinke, P.; Blum, V.; Scheffler, M. Hybrid functionals for large periodic systems in an all-electron, numeric atom-centered basis framework. *Computer Physics Communications* **2015**, *192*, 60-69.

(45) Knuth, F.; Carbogno, C.; Atalla, V.; Blum, V.; Scheffler, M. All-electron formalism for total energy strain derivatives and stress tensor components for numeric atom-centered orbitals. *Computer Physics Communications* **2015**, *190*, 33-50.

(46) Huhn, W. P.; Blum, V. One-hundred-three compound band-structure benchmark of post-self-consistent spin-orbit coupling treatments in density functional theory. *Physical Review Materials* **2017**, *1*, 033803.

(47) Perdew, J. P.; Burke, K.; Ernzerhof, M. Generalized Gradient Approximation Made Simple. *Physical Review Letters* **1996**, *77*, 3865-3868.

(48) Tkatchenko, A.; Scheffler, M. Accurate Molecular Van Der Waals Interactions from Ground-State Electron Density and Free-Atom Reference Data. *Physical Review Letters* **2009**, *102*, 073005.

(49) Liu, C.; Huhn, W.; Du, K.-Z.; Vazquez-Mayagoitia, A.; Dirkes, D.; You, W.; Kanai, Y.; Mitzi, D. B.; Blum, V. Tunable Semiconductors: Control over Carrier States and Excitations in Layered Hybrid Organic-Inorganic Perovskites. *Physical Review Letters* **2018**, *121*, 146401.

(50) Mitzi, D. B. Synthesis, Structure, and Properties of Organic-Inorganic Perovskites and Related Materials. *Progress in Inorganic Chemistry* **1999**, 1-121.

(51) Takahashi, Y.; Obara, R.; Nakagawa, K.; Nakano, M.; Tokita, J.-y.; Inabe, T. Tunable Charge Transport in Soluble Organic–Inorganic Hybrid Semiconductors. *Chemistry of Materials* **2007**, *19*, 6312-6316.

(52) Mondal, P. C.; Fontanesi, C.; Waldeck, D. H.; Naaman, R. Spin-Dependent Transport through Chiral Molecules Studied by Spin-Dependent Electrochemistry. *Accounts of Chemical Research* **2016**, *49*, 2560-2568.

(53) Naaman, R.; Waldeck, D. H. Spintronics and Chirality: Spin Selectivity in Electron Transport Through Chiral Molecules. *Annual Review of Physical Chemistry* **2015**, *66*, 263-281.

(54) Naaman, R.; Waldeck, D. H. Chiral-Induced Spin Selectivity Effect. *The Journal of Physical Chemistry Letters* **2012**, *3*, 2178-2187.

(55) Kiran, V.; Cohen, S. R.; Naaman, R. Structure dependent spin selectivity in electron transport through oligopeptides. *The Journal of Chemical Physics* **2016**, *146*, 092302.

(56) Larson, A. C. V. D., R. B. : *General Structure Analysis System*: MS-H805; LANSCE: Los Alamos, NM,, 1994.

(57) Toby, B. EXPGUI, a graphical user interface for GSAS. *Journal of Applied Crystallography* **2001**, *34*, 210-213.

(58) Sheldrick, G. SHELXT - Integrated space-group and crystal-structure determination. *Acta Crystallographica Section A* **2015**, *71*, 3-8.

(59) Dolomanov, O. V.; Bourhis, L. J.; Gildea, R. J.; Howard, J. A. K.; Puschmann, H. OLEX2: a complete structure solution, refinement and analysis program. *Journal of Applied Crystallography* **2009**, *42*, 339-341.

(60) Kortüm, G.; Braun, W.; Herzog, G. Principles and Techniques of Diffuse-Reflectance Spectroscopy. *Angewandte Chemie International Edition in English* **1963**, *2*, 333-341.

(61) Zheng, X.; Liu, M.; Johnson, E. R.; Contreras-García, J.; Yang, W. Delocalization error of density-functional approximations: A distinct manifestation in hydrogen molecular chains. *The Journal of Chemical Physics* **2012**, *137*, 214106.

(62) Egger, D. A.; Liu, Z.-F.; Neaton, J. B.; Kronik, L. Reliable Energy Level Alignment at Physisorbed Molecule–Metal Interfaces from Density Functional Theory. *Nano Letters* **2015**, *15*, 2448-2455.

(63) Heyd, J.; Scuseria, G. E.; Ernzerhof, M. Hybrid functionals based on a screened Coulomb potential. *The Journal of Chemical Physics* **2003**, *118*, 8207-8215.

(64) Heyd, J.; Scuseria, G. E.; Ernzerhof, M. Erratum: "Hybrid functionals based on a screened Coulomb potential" [J. Chem. Phys. 118, 8207 (2003)]. *The Journal of Chemical Physics* **2006**, *124*, 219906.

(65) Jana, M. K.; Janke, S. M.; Dirkes, D. J.; Dovletgeldi, S.; Liu, C.; Qin, X.; Gundogdu, K.; You, W.; Blum, V.; Mitzi, D. B. Direct-Bandgap 2D Silver–Bismuth Iodide Double Perovskite: The Structure-Directing Influence of an Oligothiophene Spacer Cation. *Journal of the American Chemical Society* **2019**, *141*, 7955-7964.

(66) Jana, M. K.; Liu, C.; Lidin, S.; Dirkes, D. J.; You, W.; Blum, V.; Mitzi, D. B. Resolving Rotational Stacking Disorder and Electronic Level Alignment in a 2D Oligothiophene-Based Lead Iodide Perovskite. *Chemistry of Materials* **2019**, *31*, 8523-8532.

ToC